Available online at www.sciencedirect.com
ScienceDirect
Comput. Methods Appl. Mech. Engrg. xxx (xxxx) xxx
Computer methods in applied mechanics and engineering
www.elsevier.com/locate/cma

Rapid simulation-based uncertainty quantification of flash-type time-of-flight and Lidar-based body-scanning processes

T.I. Zohdi

Department of Mechanical Engineering 6117 Etcheverry Hall, University of California, Berkeley, CA, 94720-1740, USA

Available online xxxx

Highlights

- Develops efficient and rapid computational method to simulate fast flash-type single-pulse Lidar.
- Method based on decomposition of a Lidar pulse into a group of rays, which are then tracked and processed.
- Identifies regions where the return signal will be erroneous due to multiple reflections.
- Allows one to quickly quantify the uncertainty in the response.

Abstract

Lidar and other time-of-flight technologies have recently received significant attention in both academic and industrial biomechanics communities, driven by technological advances in human body scanners. This paper develops an efficient and rapid computational method to simulate fast flash-type single-pulse Lidar, based on decomposition of a Lidar pulse into a group of rays, which are then tracked and processed. This allows one to quickly quantify the uncertainty in the response by identifying regions where the return signal will be erroneous due to multiple reflections.

Keywords: Lidar; Flash-type; Simulation; Uncertainty quantification

1. Introduction

Remote sensing and scanning technologies have become integral tools, which entail the acquisition of information about a surface, an object or phenomenon without making physical (mechanical) contact, primarily through a transmitted signal and a resulting reflection. In particular, optical scanning based on Lidar (light detection and ranging) and time-of-flight signal processing has become a ubiquitous technology, with many variants now being proposed. This technology has recently received large amounts of attention by the academic and industrial biomechanics communities, driven by the ongoing development of human body scanners. Applications range from 3D body scanners that can capture the entire human body quickly, for example for prosthetic designs, analysis of biomechanical movement, surface scans for tumors, fitness scans, forensic analyses, anomaly detection, generation of numerical biomechanical models (meshing) and creation of virtual reality avatars. Such technology is based on *scanning* Lidar, which produces thousands of narrow bandwidth pulses per second and scans a domain, using a signal time-of-flight analyses to determine the surface profile. Essentially, a stereographic 3D image is produced.

E-mail address: zohdi@berkeley.edu.

https://doi.org/10.1016/j.cma.2019.03.056
0045-7825/

This scanning process can be slow and time consuming. Emerging methods are pursuing *flash* Lidar, which uses a single "flash" pulse and attempts to extract information of the resulting back-scatter signal. It is much faster, but there is potentially more error due to possible multiple reflections that pollute the processing of the return signal.

This paper explores these issues by developing a fast computational method based on decomposition of the pulse into a group of rays, which are then tracked. This allows one to rapidly quantify the uncertainty by identifying regions where the signal will be erroneous and serves as a guide for practitioners to ascertain where problems may occur a priori to experiments. Specifically, this work simulates a flash pulse on an oscillatory and materially nonuniform domain. A discrete-ray model is developed in order to enable rapid assessment of the response of a surface to an incoming pulse. The pulse is decomposed into a set of discrete rays. Ray-tracking is used to calculate the propagation and reflection of the return signal. Examples are given and are comprised of initially coherent incident pulses, their propagation and subsequent scattered reflection. Basic system trends are computed, varying the surface topology and return signal fidelity. The work is motivated by the advances, within the last few decades, in the development of optically-based imaging technologies, such as Lidar. Lidar is a technique by which a target is illuminated with a laser and the reflected light is analyzed. Lidar was developed in the 1960s, and it combines laser focusing with radar-like technology for calculating distances by measuring the time for a signal to return. It enjoys a wide range of uses (see [1–6]) in the motion capture community and is a relatively standard tool in the atmospheric sciences, ranging from remote sensing, airborne laser mapping and cloud measurement, and has been extended to a variety of applications in engineering and science. *It has also started finding usage in the characterization of the human body.* Typically, Lidar uses high-frequency ultraviolet, visible and near infrared light. For reviews, we refer the reader to Ring [7], Cracknell and Hayes [8], Goyer and Watson [9], Medina et al. [10] and Trickey et al. [11].

1.1. Lidar and time-of-flight cameras

Lidar can be considered as one of a family of methods classified as "time-of-flight" cameras, whereby a pulse (optical) energy is released and the time it takes to reach the target and to return, coupled with knowledge of the propagation speed determines the relative distance. Such devices have steadily evolved for the last 20 years [12–18]. In particular, due to the large number of UAV's and aircraft available, Lidar has become quite popular as a surveying method that measures distance by illuminating the target-essentially as a 3D laser scanner. Lidar became popular in 1971 to map the moon's surface and also as a lunar altimeter. Lidar originated in the 1960s shortly after lasers were developed. The most common use of time-of-flight methods is as a Digital Elevation Model (DEM) using the concept of a point cloud using a time-of-flight calculation. A time-of-flight analysis consists of:

- Computing/measuring the total return time of a transmitted signal:

$$t^{tot} = t_1 + t_2 = \frac{d_1}{v} + \frac{d_2}{v}. \tag{1.1}$$

- Isolating the time to encounter the scatterer:

$$t_1 = \frac{d_1}{v} = t^{tot} - t_2 = t^{tot} - \frac{d_2}{v} = t^{tot} - \frac{L}{v \sin\theta}, \tag{1.2}$$

  where $\theta = \cos^{-1}\left(-\frac{\boldsymbol{v}_1 \cdot \boldsymbol{v}_2}{\|\boldsymbol{v}_1\| \|\boldsymbol{v}_2\|}\right)$.
- Calculating the distance d_1 ($\|\boldsymbol{v}_1\| = \|\boldsymbol{v}_2\| = v$) from the emitter/camera to yield:

$$d_1 = vt^{tot} - vt_2 = vt^{tot} - \frac{vL}{v \sin\theta} = vt^{tot} - \frac{L}{\sin\theta}. \tag{1.3}$$

The wavelengths used are most commonly 600–1000 nm. However, 1550 nm devices are "eye safe" (for large surface areas), but less accurate (this requires the use of gallium-arsenide, which is costly). Typical airborne topographic lasers operate at 1069 nm. Historically, they enjoy widespread use in agriculture, archaeology, etc. coupled with unmanned autonomous vehicles. This ranges from (1) Profiling Lidar, where an individual pulse is placed in a single line (2) Small footprint Lidar scans at 20 degrees back and forth (3) Large-footprint Lidar, which pulses an entire area (3) Topographical Lidar uses near infrared (4) Bathymetric Lidar, which is water penetrating

Please cite this article as: T.I. Zohdi, Rapid simulation-based uncertainty quantification of flash-type time-of-flight and Lidar-based body-scanning processes, Computer Methods in Applied Mechanics and Engineering (2019), https://doi.org/10.1016/j.cma.2019.03.056.

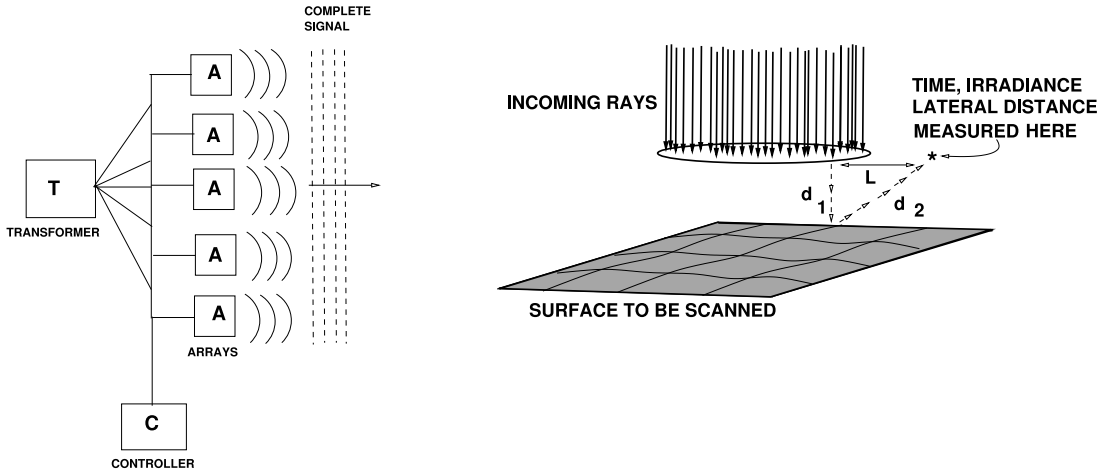

Fig. 1. Left: A phased array producing a flash pulse. Right: For mathematical analyses, a flash pulse comprised of rays, with a schematic of the hypothetical trajectory of one of the rays within the pulse.

green light to measure seafloor and riverbed elevations (5) Ground-based Lidar, where a tripod unit scans a hemisphere. The components can entail (1) Lidar sensors which scan from side to side: green light or infrared (2) GPS receivers track the altitude of the plane or UAV (3) Inertial measurements (IMU) track the tilt of the plane or UAV and (4) Computers/data recorders. There are usually two forms of signal storage: (1) Discrete Lidar stores peak return signals and (2) Full wave Lidar stores everything.

1.2. Flash lidar

Recently, because of demands for rapid scanning, "flash" methods which use a single flash pulse have started to become popular. This may require the use of phased arrays (Fig. 1), which are a collection of many individual antennas—they are inexpensive, but last about 1000–2000 h, as opposed to 100,000 h from a solid state (expensive) laser. Often, a point-cloud is generated as a result of the return signal, which comprises a set of data points in space that indicate the computed profile of the object to be scanned. This is closely related to the field of Computer Vision, which deals with how computers can be made to gain high level understanding from digital images involving topographical modeling methods for acquiring processing and analyzing digital images (a form of AI) and extraction of edges, inference, shape recognition, etc. Application examples range from automatic inspection, assisting humans, in identification, controlling processes, detecting events, computer–human interactions, navigation, object classification, medical image analysis and *body scanning*. Flash-type cameras/scanners have an advantage over more sophisticated methods because:

- The systems are simple, since they do not have moving parts associated with a scanner, and can thus be made very compact.
- The systems measure the entire surface in a single pulse, hence they are fast and can be used in real time and
- The systems do not require sophisticated post-processing units and are therefore inexpensive.

However, the greatest problems arise from multiple reflections of a pulse (Fig. 2) which can ruin time-of-flight calculations and other subsequent post processing. In this paper we construct a fast computational framework to simulate a time-of-flight flash camera and discuss the sources of error associated with multiple reflections that computational methods can help identify and possibly alleviate. The utility of this is that it allows one to rapidly identify the regions where the signal will be erroneous and to determine those regions which will need to be reconstructed by other means (this is called "registration"), and which may need to be scanned from another angle and combined with data from other scans.

Please cite this article as: T.I. Zohdi, Rapid simulation-based uncertainty quantification of flash-type time-of-flight and Lidar-based body-scanning processes, Computer Methods in Applied Mechanics and Engineering (2019), https://doi.org/10.1016/j.cma.2019.03.056.

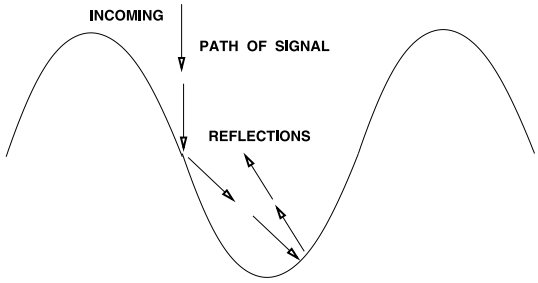

Fig. 2. Corruption of a time-of-flight signal by multiple reflections.

2. Objectives

In order to enable the ability to rapidly simulate a flash-Lidar-type system, we develop a discrete-ray model for the characterization of the response of a point-cloud surface to a coherent pulse of high-frequency energy. Specifically, the interest here is on the behavior of an initially coherent pulse (Fig. 1), represented by multiple collimated (parallel) rays (initially forming a planar wave front), where each ray is a vector in the direction of the flow of optical energy (the rays are parallel to the initial wave's propagation vector). It is assumed that the features of the surface to be scanned are at least an order of magnitude larger than the wavelength of the incident radiation (essentially specular surfaces), therefore "geometrical" ray tracing theory is applicable, and is well-suited for the systems of interest. Ray-tracing is a method that is employed to produce rapid approximate solutions to wave-equations for high-frequency/small-wavelength applications where the primary interest is in the overall propagation of energy.[1] Essentially, ray-tracing methods proceed by initially representing wave fronts by an array of discrete rays. *Thereafter, the problem becomes one of a primarily geometric character*, where one tracks the changing trajectories and magnitudes of individual rays which are dictated by the reflectivity and the Fresnel conditions (if a ray encounters a material interface). Ray-tracing methods are well-suited for computation of scattering in complex systems that are difficult to mesh/discretize, relative to procedures such as the Finite Difference Time Domain Method or the Finite Element Method. For review of the state-of-the-art in industrially-oriented optics, see Gross [19]. In the approach taken in this work, the beam is discretized into a set of rays (Fig. 1). Even in the case where this clear separation of length scales is not present, this model still provides valuable information on the propagation of the beam and the reflected response of the dispersed system.[2] An efficient discrete ray-tracking algorithm is developed to track the propagation of rays into the system. Quantitative examples are given, focusing on concentrated optical pulses, their subsequent propagation and reflection.

Remark. The regimes of validity of such a model are where the surface features are larger than visible light rays: 3.8×10^{-7} m $\leq \lambda \leq 7.2 \times 10^{-7}$ m. The features in this analysis are assumed to possess length-scales larger than approximately 10^{-5} m (10 microns). For systems with length-scales smaller than this, one can interpret the results of the model in a qualitative manner, although the range of applicability is not limited to visible frequencies. Other high frequency applications where the developed model could potentially be employed include UV-rays (10^{-9} m $\leq \lambda \leq 10^{-8}$ m), X-rays (10^{-11} m $\leq \lambda \leq 10^{-9}$ m) and gamma rays (10^{-12} m $\leq \lambda \leq 10^{-11}$ m), provided that the scattering target has the appropriate (larger) length-scale.

3. Propagation of electromagnetic energy

3.1. Decomposition of a beam into a set of rays

In order to connect the concept of a ray with a pulse/beam, since $\bar{I}$ is the energy per unit area per unit time, we obtain the energy associated with an entire pulse/beam by multiplying the irradiance by the cross-sectional area of

[1] Resolving diffraction (which ray theory is incapable of describing) is unimportant for the applications of interest.

[2] It is important to emphasize the regimes of validity of such a model are where the surface features are larger than the optical wavelengths. For example, if we were to use visible light (wavelengths between 3.8×10^{-7} m $\leq \lambda \leq 7.2 \times 10^{-7}$ m) the features in this analysis would be assumed to possess scales larger than approximately 10^{-5} m (10 microns). For systems containing features smaller than this, one can simply use the model as a qualitative guide.

Please cite this article as: T.I. Zohdi, Rapid simulation-based uncertainty quantification of flash-type time-of-flight and Lidar-based body-scanning processes, Computer Methods in Applied Mechanics and Engineering (2019), https://doi.org/10.1016/j.cma.2019.03.056.

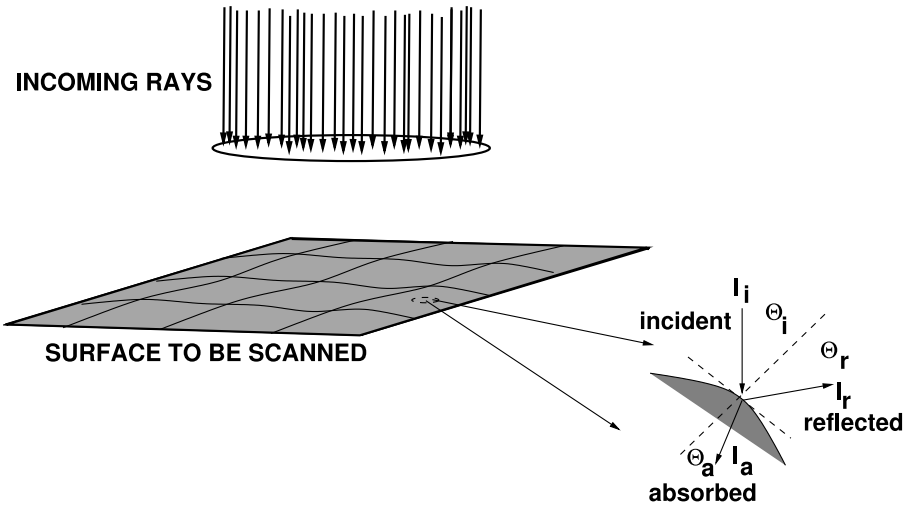

Fig. 3. An electromagnetic pulse applied to a surface.

an initially coherent beam, $\bar{I}A^b$, where A^b is the cross-sectional area of the beam (comprising all of the rays). The energy per unit time (power) for a ray in the pulse/beam is then given by

$$I = \bar{I}A^r = \bar{I}A^b/N_r, \tag{3.1}$$

where N_r is the number of rays in the beam (Fig. 3) and A^r can be considered the area associated with a ray. Essentially, rays are a mathematical construction/discretization of a pulse/beam. We refer the reader to Gross [19], Zohdi [20–25] for details.

3.2. Reflection and absorption of rays

Following a framework found in Zohdi [20–24] for details, we consider a ray of light incident upon a material interface which produces a reflected ray and a transmitted/absorbed (refracted) ray (Fig. 3), the amount of incident electromagnetic energy per unit time, power (I_i), that is reflected (I_r) is given by the total reflectance $\mathcal{IR} \stackrel{\text{def}}{=} \frac{I_r}{I_i}$, where $0 \leq \mathcal{IR} \leq 1$. $\mathcal{IR}$ is given by Eq. (3.3), for unpolarized electromagnetic radiation. The angle between the point of contact of a ray (Fig. 3) and the outward normal to the surface at that point is the angle of incidence, θ_i. The classical reflection law states that the angle at which a ray is reflected is the same as the angle of incidence and that the incoming (incident, θ_i) and outgoing (reflected, θ_r) ray lays in the same plane, and $\theta_i = \theta_r$. Furthermore, refraction law states that, if the ray passes from one medium into a second one (with a different index of refraction), and, if the index of refraction of the second medium is less than that of the first, the angle the ray makes with the normal to the interface is always less than the angle of incidence, where $\hat{n} \stackrel{\text{def}}{=} \frac{v_i}{v_a} = \sqrt{\frac{\epsilon_a \mu_a}{\epsilon_i \mu_i}} = \frac{\sin\theta_i}{\sin\theta_a}$, θ_a being the angle of the absorbed ray (Fig. 3), v_a is the propagation speed in the absorbing medium, v_i is the propagation speed in the incident medium, ϵ_a is the electric permittivity of the absorbing medium, μ_a is the magnetic permeability of the absorbing medium, ϵ_i is the electric permittivity in the incident medium and μ_i is the magnetic permeability in the incident medium. Recall, all electromagnetic radiation travels, in a vacuum, at the speed $c \approx 2.99792458 \times 10^8 \pm 1.1$ m/s. In any another medium $v = \frac{1}{\sqrt{\epsilon\mu}}$ for electromagnetic waves.[3] We define $\hat{n}$ as the ratio of the refractive indices of the ambient (incident) medium (n_i) and absorbing medium (n_a), $\hat{n} = n_a/n_i$, where $\hat{\mu}$ is the ratio of the magnetic permeabilities of the surrounding incident medium (μ_i) and scattering/absorbing medium (μ_a), $\hat{\mu} = \mu_a/\mu_i$. Thus, we have

$$\hat{n} = \frac{n_a}{n_i} = \sqrt{\frac{\epsilon_a \mu_a}{\epsilon_i \mu_i}} \Rightarrow \epsilon_a \mu_a = (\hat{n})^2 \epsilon_i \mu_i. \tag{3.2}$$

[3] The free space electric permittivity is $\epsilon_o = \frac{1}{c^2 \mu_o} = 8.8542 \times 10^{-12}\,\mathrm{C\,N^{-1}\,m^{-1}}$ and the free space magnetic permeability is $\mu_o = 4\pi \times 10^{-7}\,\mathrm{Wb\,A^{-1}\,m^{-1}} = 1.2566 \times 10^{-6}\,\mathrm{Wb\,A^{-1}\,m^{-1}}$.

Please cite this article as: T.I. Zohdi, Rapid simulation-based uncertainty quantification of flash-type time-of-flight and Lidar-based body-scanning processes, Computer Methods in Applied Mechanics and Engineering (2019), https://doi.org/10.1016/j.cma.2019.03.056.

For a pulse of light, the reflectivity $\mathcal{IR}$ can be shown to be (see [19] for example)

$$\mathcal{IR} = \frac{I_r}{I_i} = \frac{1}{2}\left(\left(\frac{\frac{\hat{n}^2}{\hat{\mu}}\cos\theta_i - (\hat{n}^2 - \sin^2\theta_i)^{\frac{1}{2}}}{\frac{\hat{n}^2}{\hat{\mu}}\cos\theta_i + (\hat{n}^2 - \sin^2\theta_i)^{\frac{1}{2}}}\right)^2 + \left(\frac{\cos\theta_i - \frac{1}{\hat{\mu}}(\hat{n}^2 - \sin^2\theta_i)^{\frac{1}{2}}}{\cos\theta_i + \frac{1}{\hat{\mu}}(\hat{n}^2 - \sin^2\theta_i)^{\frac{1}{2}}}\right)^2\right), \tag{3.3}$$

where I_i is the incoming irradiance, I_r is the reflected irradiance, $\hat{n}$ is the ratio of the refractive indices of the of absorbing (n_a) and incident media (n_i), where the refractive index is defined as the ratio of the speed of light in a vacuum (c) to that of the medium (v), where the speed of electromagnetic waves is $c = \frac{1}{\sqrt{\epsilon_o \mu_o}}$, where ϵ is the electric permittivity and μ is the magnetic permeability. We consider applications with non-magnetic media and optical frequencies where the magnetic permeability is virtually the same for both the incident medium (usually the atmosphere) and the scattering/absorbing medium. Thus, for the remainder of the work, we shall take $\hat{\mu} = 1$ ($\mu_o = \mu_i = \mu_a$), thus

$$\hat{n} = \frac{n_a}{n_i} = \sqrt{\frac{\epsilon_a \mu_a}{\epsilon_i \mu_i}} \Rightarrow \epsilon_a \mu_a = (\hat{n})^2 \epsilon_i \mu_i \Rightarrow \epsilon_a = (\hat{n})^2 \epsilon_i. \tag{3.4}$$

This yields

$$\mathcal{IR} = \frac{I_r}{I_i} = \frac{1}{2}\left(\left(\frac{\hat{n}^2\cos\theta_i - (\hat{n}^2 - \sin^2\theta_i)^{\frac{1}{2}}}{\hat{n}^2\cos\theta_i + (\hat{n}^2 - \sin^2\theta_i)^{\frac{1}{2}}}\right)^2 + \left(\frac{\cos\theta_i - (\hat{n}^2 - \sin^2\theta_i)^{\frac{1}{2}}}{\cos\theta_i + (\hat{n}^2 - \sin^2\theta_i)^{\frac{1}{2}}}\right)^2\right). \tag{3.5}$$

Notice that as $\hat{n} \to 1$ we have complete absorption, while as $\hat{n} \to \infty$ we have complete reflection. The total amount of absorbed power by the material is $(1 - \mathcal{IR})I_i$. The next section supplies the theory underpinning electromagnetic wave propagation and rays.

4. Theory underpinning electromagnetic wave propagation and rays

Following a framework found in Zohdi [20–24], the propagation of electromagnetic waves in free space can be described by a simplified form of Maxwell's equations (see Jackson [26], Zohdi [22])

$$\nabla \times \boldsymbol{E} = -\mu_o \frac{\partial \boldsymbol{H}}{\partial t}, \qquad \text{and} \qquad \nabla \times \boldsymbol{H} = \epsilon_o \frac{\partial \boldsymbol{E}}{\partial t}, \tag{4.1}$$

where $\nabla \cdot \boldsymbol{H} = 0$, $\nabla \cdot \boldsymbol{E} = 0$, $\boldsymbol{E}$ is the electric field, $\boldsymbol{H}$ is the magnetic field, ϵ_o is the free space permittivity and μ_o is the free space permeability. Using standard vector identities, one can show that

$$\nabla \times (\nabla \times \boldsymbol{E}) = -\mu_o \epsilon_o \frac{\partial^2 \boldsymbol{E}}{\partial t^2}, \qquad \text{and} \qquad \nabla \times (\nabla \times \boldsymbol{H}) = -\mu_o \epsilon_o \frac{\partial^2 \boldsymbol{H}}{\partial t^2}, \tag{4.2}$$

and that

$$\nabla^2 \boldsymbol{E} = \frac{1}{c^2}\frac{\partial^2 \boldsymbol{E}}{\partial t^2}, \qquad \text{and} \qquad \nabla^2 \boldsymbol{H} = \frac{1}{c^2}\frac{\partial^2 \boldsymbol{H}}{\partial t^2}, \tag{4.3}$$

where the speed of electromagnetic waves is $c = \frac{1}{\sqrt{\epsilon_o \mu_o}}$. All electromagnetic radiation travels, in a vacuum, at the speed $c \approx 2.99792458 \times 10^8 \pm 1.1$ m/s. In any another medium, for electromagnetic waves, the propagation speed is $v = \frac{1}{\sqrt{\epsilon \mu}}$, where ϵ and μ are the electric permittivity and magnetic permeability of that medium, respectively.[4]

4.1. Plane harmonic wave fronts

Now consider the special case of plane harmonic waves, for example of the form

$$\boldsymbol{E} = \boldsymbol{E}_o \cos(\boldsymbol{k} \cdot \boldsymbol{x} - \omega t) \qquad \text{and} \qquad \boldsymbol{H} = \boldsymbol{H}_o \cos(\boldsymbol{k} \cdot \boldsymbol{x} - \omega t), \tag{4.4}$$

where $\boldsymbol{x}$ is an initial position vector to the wave front, where $\boldsymbol{k}$ is the direction of propagation. We refer to the phase as $\phi = \boldsymbol{k} \cdot \boldsymbol{x} - \omega t$, and $\omega = \frac{2\pi}{\tau}$ as the angular frequency, where τ is the period. For plane waves, the wave front

[4] The free space electric permittivity is $\epsilon_o = \frac{1}{c^2 \mu_o} = 8.8542 \times 10^{-12}\ \mathrm{C\,N^{-1}\,m^{-1}}$ and the free space magnetic permeability is $\mu_o = 4\pi \times 10^{-7}\ \mathrm{Wb\,A^{-1}\,m^{-1}} = 1.2566 \times 10^{-6}\ \mathrm{Wb\,A^{-1}\,m^{-1}}$.

Please cite this article as: T.I. Zohdi, Rapid simulation-based uncertainty quantification of flash-type time-of-flight and Lidar-based body-scanning processes, Computer Methods in Applied Mechanics and Engineering (2019), https://doi.org/10.1016/j.cma.2019.03.056.

is a plane on which ϕ is constant, which is orthogonal to the direction of propagation, characterized by $\boldsymbol{k}$. In the case of harmonic waves, we have

$$\boldsymbol{k} \times \boldsymbol{E} = \mu_o \omega \boldsymbol{H} \qquad \text{and} \qquad \boldsymbol{k} \times \boldsymbol{H} = -\epsilon_o \omega \boldsymbol{E}, \tag{4.5}$$

and $\boldsymbol{k} \cdot \boldsymbol{E} = 0$ and $\boldsymbol{k} \cdot \boldsymbol{H} = 0$. The three vectors, $\boldsymbol{k}$, $\boldsymbol{E}$ and $\boldsymbol{H}$ constitute a mutually orthogonal triad.[5] The direction of wave propagation is given by $\frac{\boldsymbol{E}\times\boldsymbol{H}}{\|\boldsymbol{E}\times\boldsymbol{H}\|}$. Electromagnetic waves traveling through space carry electromagnetic energy which flows in the direction of wave propagation. The energy per unit area per unit time flowing perpendicularly into a surface in free space is given by the Poynting vector $\boldsymbol{S} = \boldsymbol{E} \times \boldsymbol{H}$.

4.2. Special case: natural (random) electromagnetic energy propagation

Since at high-frequencies $\boldsymbol{E}$, $\boldsymbol{H}$ and $\boldsymbol{S}$ oscillate rapidly, it is impractical to measure instantaneous values of $\boldsymbol{S}$ directly. Consider the harmonic representations in Eq. (4.4) which leads to $\boldsymbol{S} = \boldsymbol{E}_o \times \boldsymbol{H}_o \cos^2(\boldsymbol{k} \cdot \boldsymbol{x} - \omega t)$, and consequently the average value over a longer time interval ($\mathcal{T}$) than the time scale of rapid random oscillation,

$$\langle \boldsymbol{S} \rangle_{\mathcal{T}} = \boldsymbol{E}_o \times \boldsymbol{H}_o \langle \cos^2(\boldsymbol{k} \cdot \boldsymbol{x} - \omega t) \rangle_{\mathcal{T}} = \tfrac{1}{2} \boldsymbol{E}_o \times \boldsymbol{H}_o, \tag{4.6}$$

leading to the definition of the *irradiance*

$$I \stackrel{\text{def}}{=} \langle \|\boldsymbol{S}\| \rangle_{\mathcal{T}} = \tfrac{1}{2} \|\boldsymbol{E}_o \times \boldsymbol{H}_o\| = \tfrac{1}{2} \sqrt{\tfrac{\epsilon_o}{\mu_o}} \|\boldsymbol{E}_o\|^2. \tag{4.7}$$

Thus, the rate of flow of energy is proportional to the square of the amplitude of the electric field.

4.3. Reflection and absorption of energy-Fresnel relations

We consider a plane harmonic wave incident upon a plane boundary separating two different materials, specifically vacuum and surface, which produces a reflected wave and an absorbed (refracted) wave (Fig. 3). Two cases for the electric field vector are considered: (1) electric field vectors that are parallel ($\|$) to the plane of incidence and (2) electric field vectors that are perpendicular ($\perp$) to the plane of incidence. In either case, the tangential components of the electric and magnetic fields are required to be continuous across the interface. Consider case (1). We have the following general vectorial representations:

$$\boldsymbol{E}_{\|} = E_{\|} \cos(\boldsymbol{k} \cdot \boldsymbol{x} - \omega t)\, \boldsymbol{e}_1 \qquad \text{and} \qquad \boldsymbol{H}_{\|} = H_{\|} \cos(\boldsymbol{k} \cdot \boldsymbol{x} - \omega t)\, \boldsymbol{e}_2, \tag{4.8}$$

where $\boldsymbol{e}_1$ and $\boldsymbol{e}_2$ are orthogonal to the propagation direction $\boldsymbol{k}$. By employing the law of refraction ($n_i \sin\theta_i = n_a \sin\theta_a$) we obtain the following conditions relating the incident, reflected and absorbed components of the electric field quantities:

$$E_{\|i} \cos\theta_i - E_{\|r} \cos\theta_r = E_{\|a} \cos\theta_a \qquad \text{and} \qquad H_{\perp i} + H_{\perp r} = H_{\perp a}. \tag{4.9}$$

Since, for plane harmonic waves, the magnetic and electric field amplitudes are related by $H = \frac{E}{v\mu}$, we have

$$E_{\|i} + E_{\|r} = \frac{\mu_i}{\mu_a} \frac{v_i}{v_a} E_{\|a} = \frac{\mu_i}{\mu_a} \frac{n_a}{n_i} E_{\|a} \stackrel{\text{def}}{=} \frac{\hat{n}}{\hat{\mu}} E_{\|a}, \tag{4.10}$$

where $\hat{\mu} \stackrel{\text{def}}{=} \frac{\mu_a}{\mu_i}$, $\hat{n} \stackrel{\text{def}}{=} \frac{n_a}{n_i}$ and where v_i, v_r and v_a are the values of the velocity in the incident, reflected and absorbed directions.[6] By again employing the law of refraction, we obtain the Fresnel reflection and transmission/absorption coefficients, generalized for the case of unequal magnetic permeabilities

$$r_{\|} = \frac{E_{\|r}}{E_{\|i}} = \frac{\frac{\hat{n}}{\hat{\mu}} \cos\theta_i - \cos\theta_a}{\frac{\hat{n}}{\hat{\mu}} \cos\theta_i + \cos\theta_a} \qquad \text{and} \qquad a_{\|} = \frac{E_{\|a}}{E_{\|i}} = \frac{2\cos\theta_i}{\cos\theta_a + \frac{\hat{n}}{\hat{\mu}} \cos\theta_i}. \tag{4.11}$$

Following the same procedure for case (2), where the components of $\boldsymbol{E}$ are perpendicular to the plane of incidence, we have

$$r_{\perp} = \frac{E_{\perp r}}{E_{\perp i}} = \frac{\cos\theta_i - \frac{\hat{n}}{\hat{\mu}} \cos\theta_a}{\cos\theta_i + \frac{\hat{n}}{\hat{\mu}} \cos\theta_a} \qquad \text{and} \qquad a_{\perp} = \frac{E_{\perp a}}{E_{\perp i}} = \frac{2\cos\theta_i}{\cos\theta_i + \frac{\hat{n}}{\hat{\mu}} \cos\theta_a}. \tag{4.12}$$

[5] By combining the relations in Eq. (4.5) one obtains $\|\boldsymbol{k}\| = \frac{\omega}{c}$.

[6] Throughout the analysis we assume that $\hat{n} \geq 1$.

Please cite this article as: T.I. Zohdi, Rapid simulation-based uncertainty quantification of flash-type time-of-flight and Lidar-based body-scanning processes, Computer Methods in Applied Mechanics and Engineering (2019), https://doi.org/10.1016/j.cma.2019.03.056.

Our primary interest is in the reflections. We define the reflectances as

$$\mathcal{IR}_{\parallel} \stackrel{\text{def}}{=} r_{\parallel}^2 \qquad \text{and} \qquad \mathcal{IR}_{\perp} \stackrel{\text{def}}{=} r_{\perp}^2. \tag{4.13}$$

Particularly convenient forms for the reflections are

$$r_{\parallel} = \frac{\frac{\hat{n}^2}{\hat{\mu}}\cos\theta_i - (\hat{n}^2 - \sin^2\theta_i)^{\frac{1}{2}}}{\frac{\hat{n}^2}{\hat{\mu}}\cos\theta_i + (\hat{n}^2 - \sin^2\theta_i)^{\frac{1}{2}}} \qquad \text{and} \qquad r_{\perp} = \frac{\cos\theta_i - \frac{1}{\hat{\mu}}(\hat{n}^2 - \sin^2\theta_i)^{\frac{1}{2}}}{\cos\theta_i + \frac{1}{\hat{\mu}}(\hat{n}^2 - \sin^2\theta_i)^{\frac{1}{2}}}. \tag{4.14}$$

Thus, the total energy reflected can be characterized by

$$\mathcal{IR} \stackrel{\text{def}}{=} \left(\frac{E_r}{E_i}\right)^2 = \frac{E_{\perp r}^2 + E_{\parallel r}^2}{E_i^2} = \frac{I_{\parallel r} + I_{\perp r}}{I_i}. \tag{4.15}$$

If the resultant plane of oscillation of the (polarized) wave makes an angle of γ_i with the plane of incidence, then

$$E_{\parallel i} = E_i \cos\gamma_i \qquad \text{and} \qquad E_{\perp i} = E_i \sin\gamma_i, \tag{4.16}$$

and it follows from the previous definition of I that

$$I_{\parallel i} = I_i \cos^2\gamma_i \qquad \text{and} \qquad I_{\perp i} = I_i \sin^2\gamma_i. \tag{4.17}$$

Substituting these expressions back into the expressions for the reflectances yields

$$\mathcal{IR} = \frac{I_{\parallel r}}{I_i}\cos^2\gamma_i + \frac{I_{\perp r}}{I_i}\sin^2\gamma_i = \mathcal{IR}_{\parallel}\cos^2\gamma_i + \mathcal{IR}_{\perp}\sin^2\gamma_i. \tag{4.18}$$

For natural or unpolarized electromagnetic radiation, the angle γ_i varies rapidly in a random manner, as does the field amplitude. Thus, since

$$\langle\cos^2\gamma_i(t)\rangle_{\mathcal{T}} = \tfrac{1}{2} \qquad \text{and} \qquad \langle\sin^2\gamma_i(t)\rangle_{\mathcal{T}} = \tfrac{1}{2}, \tag{4.19}$$

and therefore for natural electromagnetic radiation

$$I_{\parallel i} = \tfrac{I_i}{2} \qquad \text{and} \qquad I_{\perp i} = \tfrac{I_i}{2}. \tag{4.20}$$

and therefore

$$r_{\parallel}^2 = \frac{E_{\parallel r}^2}{E_{\parallel i}^2} = \frac{I_{\parallel r}}{I_{\parallel i}} \qquad \text{and} \qquad r_{\perp}^2 = \frac{E_{\perp r}^2}{E_{\perp i}^2} = \frac{I_{\perp r}}{I_{\perp i}}. \tag{4.21}$$

Thus, the total reflectance becomes

$$\mathcal{IR} = \frac{1}{2}(\mathcal{IR}_{\parallel} + \mathcal{IR}_{\perp}) = \frac{1}{2}(r_{\parallel}^2 + r_{\perp}^2), \tag{4.22}$$

where $0 \leq \mathcal{IR} \leq 1$. For the cases where $\sin\theta_a = \frac{\sin\theta_i}{\hat{n}} > 1$, one may rewrite reflection relations as

$$r_{\parallel} = \frac{\frac{\hat{n}^2}{\hat{\mu}}\cos\theta_i - j(\sin^2\theta_i - \hat{n}^2)^{\frac{1}{2}}}{\frac{\hat{n}^2}{\hat{\mu}}\cos\theta_i + j(\sin^2\theta_i - \hat{n}^2)^{\frac{1}{2}}} \qquad \text{and} \qquad r_{\perp} = \frac{\cos\theta_i - \frac{1}{\hat{\mu}}j(\sin^2\theta_i - \hat{n}^2)^{\frac{1}{2}}}{\cos\theta_i + \frac{1}{\hat{\mu}}j(\sin^2\theta_i - \hat{n}^2)^{\frac{1}{2}}}, \tag{4.23}$$

where $j = \sqrt{-1}$, and in this complex case[7]

$$\mathcal{IR}_{\parallel} \stackrel{\text{def}}{=} r_{\parallel}\bar{r}_{\parallel} = 1, \qquad \text{and} \qquad \mathcal{IR}_{\perp} \stackrel{\text{def}}{=} r_{\perp}\bar{r}_{\perp} = 1, \tag{4.24}$$

where $\bar{r}_{\parallel}$ and $\bar{r}_{\perp}$ are complex conjugates. Thus, for angles above the critical angle θ_i^*, all of the energy is reflected. Notice that as $\hat{n} \to 1$ we have complete absorption, while as $\hat{n} \to \infty$ we have complete reflection. The amount of absorbed irradiance by the surface is $I_a = (1 - \mathcal{IR})I_i$.

[7] The limiting case $\frac{\sin\theta_i^*}{\hat{n}} = 1$ is the critical angle (θ_i^*) case.

Please cite this article as: T.I. Zohdi, Rapid simulation-based uncertainty quantification of flash-type time-of-flight and Lidar-based body-scanning processes, Computer Methods in Applied Mechanics and Engineering (2019), https://doi.org/10.1016/j.cma.2019.03.056.

4.4. Reflectivity

To observe the dependency of $\mathcal{IR}$ on $\hat{n}$ and θ_i we can explicitly write

$$\mathcal{IR} = \frac{1}{2}\left(\left(\frac{\frac{\hat{n}^2}{\hat{\mu}}\cos\theta_i - (\hat{n}^2 - \sin^2\theta_i)^{\frac{1}{2}}}{\frac{\hat{n}^2}{\hat{\mu}}\cos\theta_i + (\hat{n}^2 - \sin^2\theta_i)^{\frac{1}{2}}}\right)^2 + \left(\frac{\cos\theta_i - \frac{1}{\hat{\mu}}(\hat{n}^2 - \sin^2\theta_i)^{\frac{1}{2}}}{\cos\theta_i + \frac{1}{\hat{\mu}}(\hat{n}^2 - \sin^2\theta_i)^{\frac{1}{2}}}\right)^2\right). \tag{4.25}$$

Clearly, as $\hat{n} \to \infty$, $\mathcal{IR} \to 1$, no matter what the angle of incidence's value. We note that as $\hat{n} \to 1$, provided that $\hat{\mu} = 1$, $\mathcal{IR} \to 0$, i.e. all incident energy is absorbed (it is transparent). With increasing $\hat{n}$, the angle for minimum reflectance grows larger. As mentioned previously, for the remainder of the work, we shall take $\hat{\mu} = 1$ ($\mu_o = \mu_i = \mu_a$), thus

$$\hat{n} = \frac{n_a}{n_i} = \sqrt{\frac{\epsilon_a \mu_a}{\epsilon_i \mu_i}} \Rightarrow \epsilon_a \mu_a = (\hat{n})^2 \epsilon_i \mu_i \Rightarrow \epsilon_a = (\hat{n})^2 \epsilon_i. \tag{4.26}$$

This yields

$$\mathcal{IR} = \frac{I_r}{I_i} = \frac{1}{2}\left(\left(\frac{\hat{n}^2\cos\theta_i - (\hat{n}^2 - \sin^2\theta_i)^{\frac{1}{2}}}{\hat{n}^2\cos\theta_i + (\hat{n}^2 - \sin^2\theta_i)^{\frac{1}{2}}}\right)^2 + \left(\frac{\cos\theta_i - (\hat{n}^2 - \sin^2\theta_i)^{\frac{1}{2}}}{\cos\theta_i + (\hat{n}^2 - \sin^2\theta_i)^{\frac{1}{2}}}\right)^2\right). \tag{4.27}$$

For more details, we refer the reader to the relatively recent treatise of Gross [19].

Remark. We now recall Eq. (3.1) that connects the concept of a ray with a pulse/beam. As mentioned before, since $\bar{I}$ is the energy per unit area per unit time, we obtain the energy associated with an entire pulse/beam by multiplying the irradiance by the cross-sectional area of an initially coherent beam, $\bar{I}A^b$, where A^b is the cross-sectional area of the beam (comprising all of the rays). The energy per unit time (power) for a ray in the pulse/beam is then given by $I = \bar{I}A^r = \bar{I}A^b/N_r$, where N_r is the number of rays in the beam (Fig. 3) and A^r can be considered the area associated with a ray. The reflection relation, Eq. (4.25), can then be used to compute changes in the magnitude of the reflected rays (and the amount absorbed), with directional changes given by the laws of reflection. We refer the reader to Gross [19], Zohdi [20–25] for details.

5. Model problem and response trends

From this point forth, we assume that the ambient medium behaves as a vacuum. Accordingly, there are no energetic losses as the rays move through the surrounding medium. Furthermore, we assume that the absorbed portion of a ray that enters the surface is not re-emitted.

5.1. Tracking of beam decomposed rays

Starting at $t = 0$ and ending at $t = T$, the simple overall algorithm to track rays is as follows, at each time increment:

1. Check for intersections of rays with surfaces (hence a reflection), and compute the ray magnitudes and orientation if there are reflections (for all rays that are experiencing a reflection, I_j^{ref}, $j = 1, 2, \ldots, Rays$),
2. Increment all ray positions ($\boldsymbol{r}_j(t + \Delta t) = \boldsymbol{r}_j(t) + \Delta t \boldsymbol{v}_j(t)$, $j = 1, 2, \ldots, Rays$),
3. Increment time forward ($t = t + \Delta t$) and repeat the process for the next time interval.

Observation. In order to capture all of the ray reflections that occur, the time step size Δt is dictated by the offset height of the scanner. A somewhat ad-hoc approach is to scale the time step size by the speed of ray propagation according to $\Delta t = \xi \frac{\mathcal{H}}{\|\boldsymbol{v}\|}$, where $\mathcal{H}$ is the height of the scanner and $0.0001 \leq \xi \leq 0.01$. Typically, the results are insensitive to ξ that are smaller than this range. Although outside the scope of this work, one can also use this algorithm to compute the thermal response by combining it with heat transfer equations via staggering schemes (Zohdi [20,22]).

Please cite this article as: T.I. Zohdi, Rapid simulation-based uncertainty quantification of flash-type time-of-flight and Lidar-based body-scanning processes, Computer Methods in Applied Mechanics and Engineering (2019), https://doi.org/10.1016/j.cma.2019.03.056.

5.2. Test surface: parametrization and surface normals

If we consider a surface to be scanned, $F(x_1, x_2, x_3) = 0$, the outward surface normals, $\boldsymbol{n}$, needed during the scattering calculations, are easy to characterize by writing $\boldsymbol{n} = \frac{\nabla F}{\|\nabla F\|}$. The components of the gradient are $\nabla F = \frac{\partial F}{\partial x_1}\boldsymbol{e}_1 + \frac{\partial F}{\partial x_2}\boldsymbol{e}_2 + \frac{\partial F}{\partial x_3}\boldsymbol{e}_3$. It is advantageous to write the surface in parametric form:

$$F(x_1, x_2, x_3) = G(x_1, x_2) - x_3 = 0. \tag{5.1}$$

which leads to

$$x_3 = G(x_1, x_2). \tag{5.2}$$

The gradient becomes

$$\nabla F = \frac{\partial G}{\partial x_1}\boldsymbol{e}_1 + \frac{\partial G}{\partial x_2}\boldsymbol{e}_2 - \boldsymbol{e}_3. \tag{5.3}$$

Observation: It is convenient to determine whether a ray has made contact with a surface domain by checking if the x_3 position of a ray is less that x_3 of the surface.

5.3. Material identification: refractive index reconstruction from the point-cloud

A starting guess for the value of $\hat{n}$ that manifests the observed $\mathcal{IR}$ is possible for the $\theta_i = 0$ expression for $\mathcal{IR}$ (Eq. (3.5))

$$\mathcal{IR}(\theta_i = 0) = (\tfrac{\hat{n}-1}{\hat{n}+1})^2 \Rightarrow \hat{n} = \tfrac{\mathcal{IR}^{1/2}-1}{1+\mathcal{IR}^{1/2}} = \hat{n}_{k=0}. \tag{5.4}$$

This provides an underestimate for the correct value of $\hat{n}$, since in the $\theta_i \geq 0$ expressions, $\hat{n}$ has to be greater to compensate for the sines and cosines in the expression. Thus, from this initial estimate value, one can increase the values of $\hat{n}_k = \hat{n}_{k-1} + \delta\hat{n}$ for $k = 1, 2, \ldots$ until the error between the computed value of $\mathcal{IR}$ and the analytical expression for $\mathcal{IR}(\hat{n})$

$$\mathcal{E}_k = |\mathcal{IR} - \tfrac{1}{2}\left(\left(\frac{\hat{n_k}^2\cos\theta_i - (\hat{n_k}^2 - \sin^2\theta_i)^{\frac{1}{2}}}{\hat{n_k}^2\cos\theta_i + (\hat{n_k}^2 - \sin^2\theta_i)^{\frac{1}{2}}}\right)^2 + \left(\frac{\cos\theta_i - (\hat{n_k}^2 - \sin^2\theta_i)^{\frac{1}{2}}}{\cos\theta_i + (\hat{n_k}^2 - \sin^2\theta_i)^{\frac{1}{2}}}\right)^2\right)|, \tag{5.5}$$

is below an error tolerance ($\mathcal{E}_k \leq tol$). Once one ascertains $\hat{n}$ for a point in the point-cloud, one can identify the material property ($\hat{n}$).

6. Numerical/quantitative examples

The discrete-ray approach is flexible enough to simulate a wide variety of systems. The initial velocity vector for all initially collimated (parallel) rays comprising the beam was $\boldsymbol{v} = (c, 0, 0)$, where $c = 3 \times 10^8$ m/s is the speed of light in a vacuum. We used a parametrized test surface given by

$$x_3 = 2 + A(\sin\frac{2\omega_1\pi x_1}{L_1})\sin(\frac{2\omega_2\pi x_2}{L_2}), \tag{6.1}$$

with $L_1 = L_2 = 1$, $\omega_1 = 1.5$ and $\omega_2 = 0.75$, where we vary A. We also used a parametrized test refractive index ratio:

$$\hat{n} = \mathcal{N}(x_1, x_2) = \hat{n}_o(1 + B\sin(\frac{2\omega_1\pi x_1}{L_1})\sin(\frac{2\omega_2\pi x_2}{L_2})), \tag{6.2}$$

with $\hat{n}_o = 5$, where $B = 0.25$. We steadily increased the number of rays in the beam from $N_r = 100, 200, etc$ until the results were insensitive to further refinements. This approach indicated that between approximately $9500 \leq N_r \leq 10{,}000$ parallel rays in the circular cross-sectional plane of the beam (randomly placed within the beam, Figs. 3 and 4), corresponding to unpolarized incoming optical energy, yielded stable results across the parameter study range.[8] Therefore, we consider the responses to be, for all practical purposes, independent of the

[8] We repeatedly refined the "ray density" up to 10,000 rays and found no significant difference beyond the 10,000 ray simulation results.

Please cite this article as: T.I. Zohdi, Rapid simulation-based uncertainty quantification of flash-type time-of-flight and Lidar-based body-scanning processes, Computer Methods in Applied Mechanics and Engineering (2019), https://doi.org/10.1016/j.cma.2019.03.056.

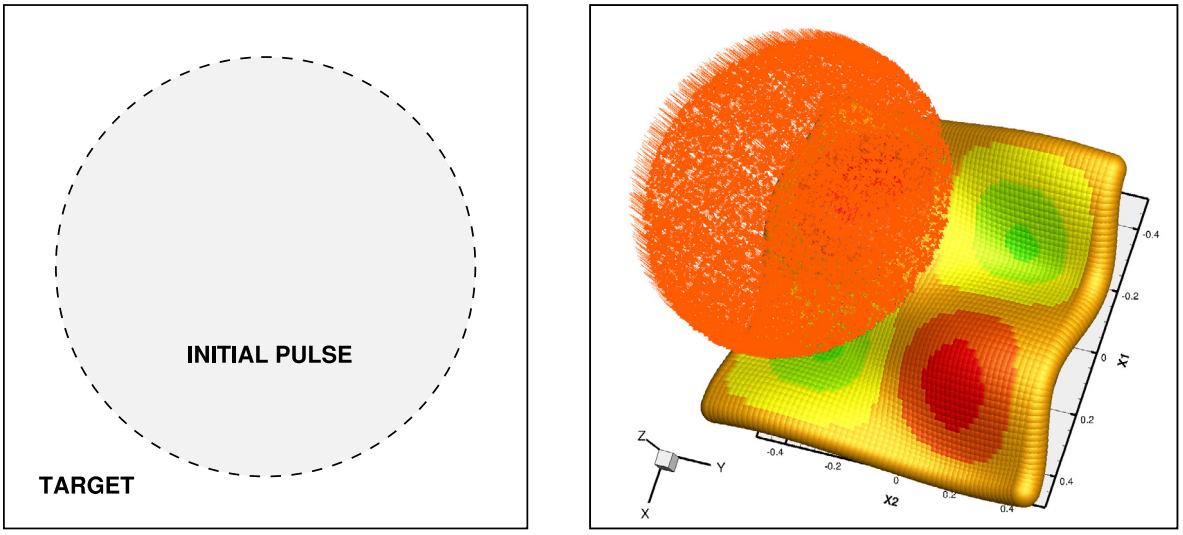

Fig. 4. Left: schematic top view of the initial pulse. Right: the numerical model. (For interpretation of the references to color in this figure legend, the reader is referred to the web version of this article.)

ray density. This surface/ray system provided convergent results, i.e. increasing the number of rays in the beam resulted in negligibly different overall system responses. The radius of the beam was $0.5L_1$ $\mathcal{R}_c$. Fig. 5 shows a sequence of frames of the detailed response of a surface to 10,000 rays. If there is no error, i.e. multiple reflections, each ray will undergo one reflection. Thus, we define the error as

$$ERROR = \frac{(RELEASED\ RAYS) - (VALID\ RETURN\ RAYS)}{(RELEASED\ RAYS)} \tag{6.3}$$

The colors of the surface indicate the reflectivity of the surface, which can then be post-processed to ascertain the refractive index and the subsequent material via Eq. (5.5). Table 1 shows the increase in the error, while Figs. 5 and 6 give an easy to read graphical result, for example for $A = 0.1$. For reference, $A = 0$ is shown, which produces no error (Fig. 7). The increase in error increases with amplitude of oscillation. Multiple reflections of a ray indicate that the time of flight analysis will be inaccurate/inapplicable. Use of return signal data from multiple reflections will lead to erroneous surface reconstruction (discontinuities). In these cases, those regions would need to be interpolated from surrounding valid regions or scanned from other angles. They cannot be constructed directly from a single flash-pulse point-cloud. This occurs at approximately $A = 0.08$. At approximately $A = 0.64$, the error is maximized.

Remark. In such a direct numerical approach, one can easily introduce nonuniform beam profiles such as

$$I(d) = I(d = 0)e^{-ad}, \tag{6.4}$$

where d is the distance from the center of the initial beam line. In the case of $a = 0$ we recapture a flat beam, $I(d) = I(d = 0)$. We can set the total initial irradiance via $\sum_{i=1}^{N_r} I_i^{inc}(t = 0)\mathcal{A}_r = P$ Watts.[9]

7. Summary and discussion

Because Lidar and other time-of-flight methods are becoming widely used in industry, with many variants being proposed, fast computational analysis and design tools are needed. Accordingly, this work developed a discrete-ray model to allow for propagation of optical energy encountering a surface. The approach provides a simpler alternative to a direct computationally intensive discretization of a continuum description employing Maxwell's equations.

[9] To achieve this distribution, one would first place rays randomly in the plane, and then scale the individual I^{inc} by e^{-ad} and the normalized average so that the total was P watts.

Please cite this article as: T.I. Zohdi, Rapid simulation-based uncertainty quantification of flash-type time-of-flight and Lidar-based body-scanning processes, Computer Methods in Applied Mechanics and Engineering (2019), https://doi.org/10.1016/j.cma.2019.03.056.

Table 1
The increase in error with amplitude of oscillation. Multiple reflections of a ray indicate that the time of flight analysis will be inaccurate/inapplicable. Use of return signal data from multiple reflections will lead to erroneous surface reconstruction (discontinuities). In these cases, those regions would need to be interpolated from surrounding valid regions or scanned from other angles. They cannot be constructed directly from a single flash-pulse point-cloud.

A	$ERROR$
0.00	0.0000
0.01	0.0000
0.02	0.0000
0.04	0.0000
0.08	0.2032
0.16	0.7908
0.32	0.9555
0.64	0.9887

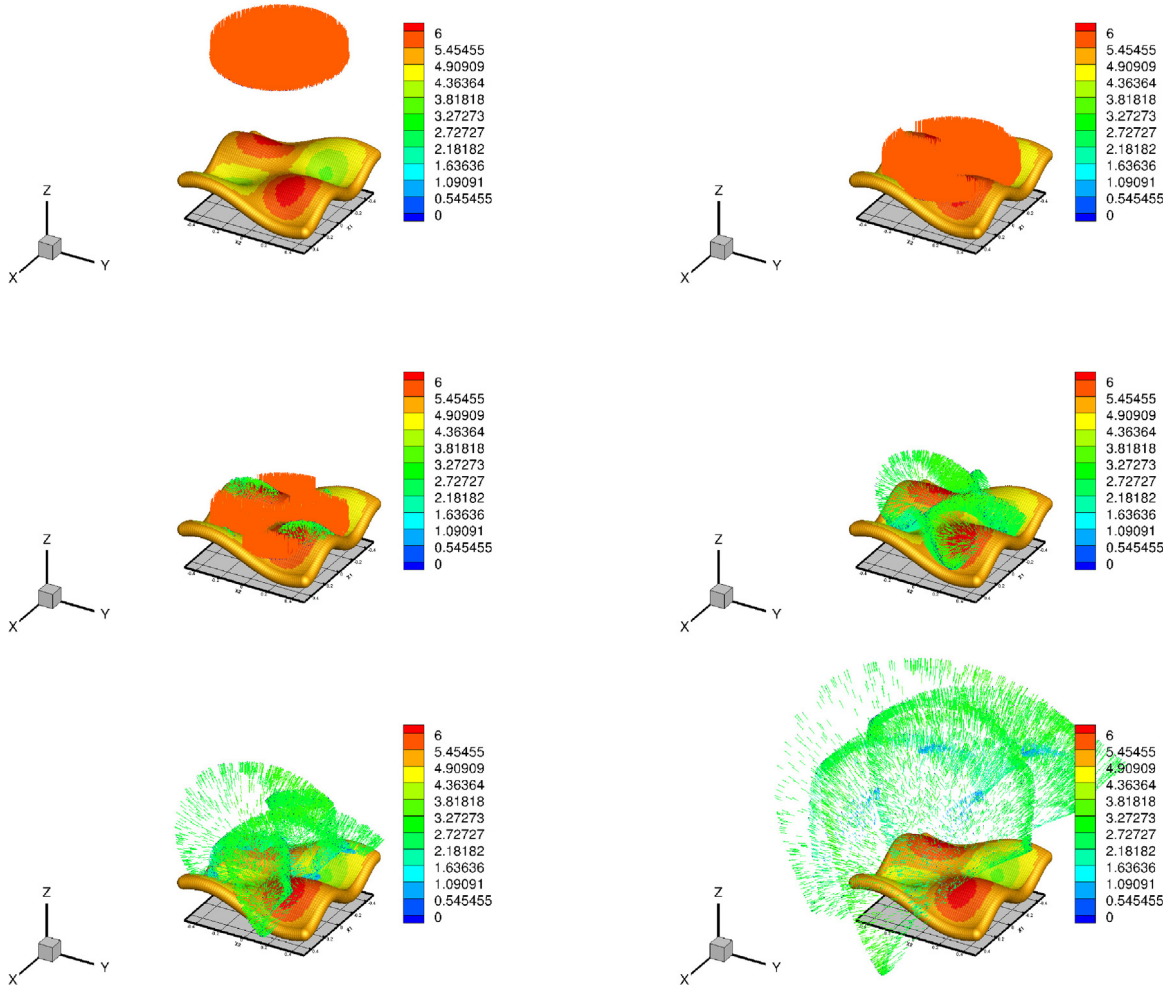

Fig. 5. Sequence of Lidar pulses for a surface with $A = 0.1$. The colors indicate the refractive index. (For interpretation of the references to color in this figure legend, the reader is referred to the web version of this article.)

Please cite this article as: T.I. Zohdi, Rapid simulation-based uncertainty quantification of flash-type time-of-flight and Lidar-based body-scanning processes, Computer Methods in Applied Mechanics and Engineering (2019), https://doi.org/10.1016/j.cma.2019.03.056.

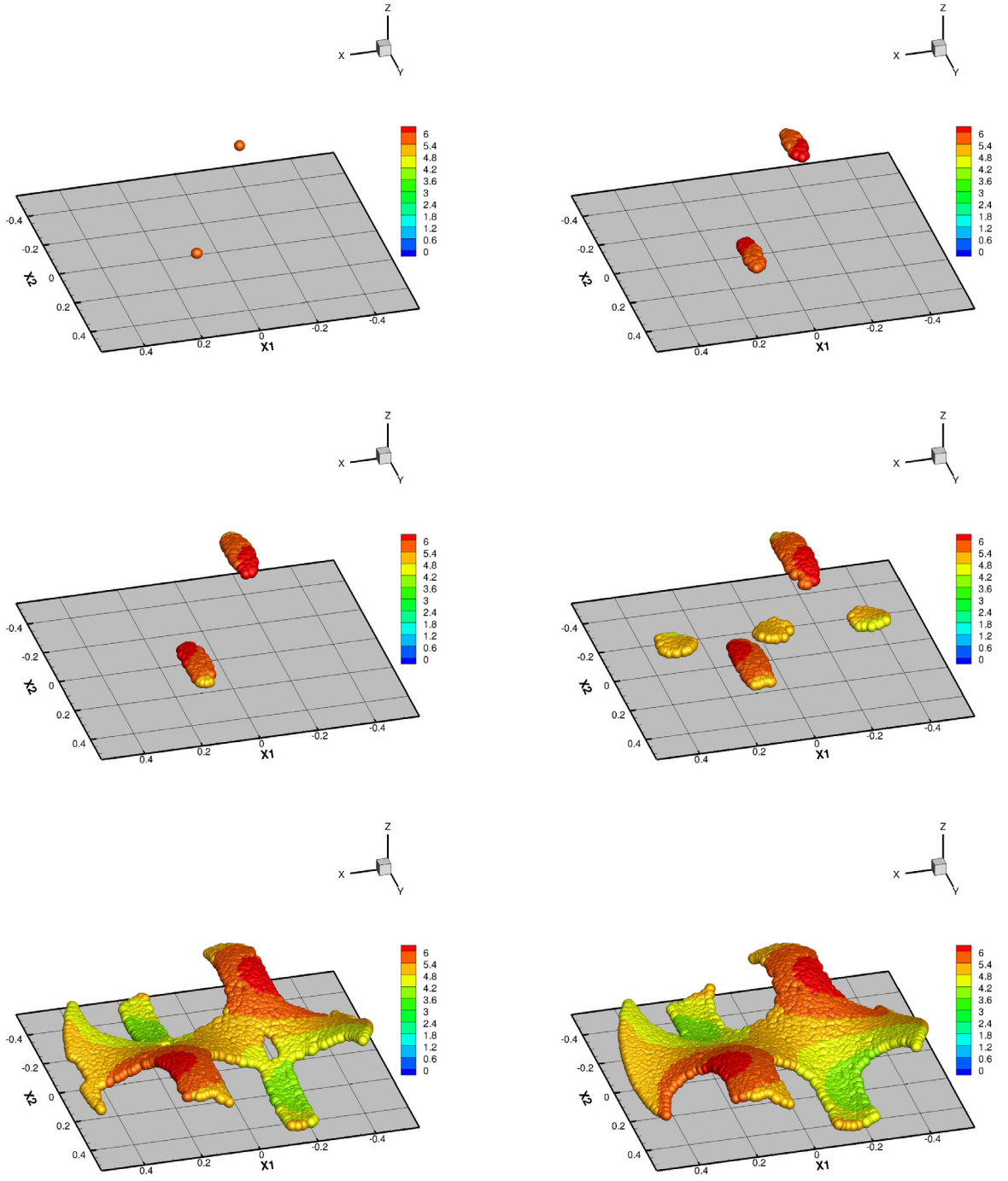

Fig. 6. Sequence of point-cloud digital elevation model for a surface of $A = 0.1$. The colors indicate the *computed* refractive index. (For interpretation of the references to color in this figure legend, the reader is referred to the web version of this article.)

Classical *scanning* Lidar produces thousands of narrow bandwidth pulses per second and scans a domain. This scanning process can be time consuming. Flash Lidar uses a single "flash" pulse and attempts to extract information from the resulting back-scatter signal, using a time-of-flight analyses. It is much faster, but there is potentially more error due to possible multiple reflections that pollute the processing of the return signal. Because of complex surfaces

Please cite this article as: T.I. Zohdi, Rapid simulation-based uncertainty quantification of flash-type time-of-flight and Lidar-based body-scanning processes, Computer Methods in Applied Mechanics and Engineering (2019), https://doi.org/10.1016/j.cma.2019.03.056.

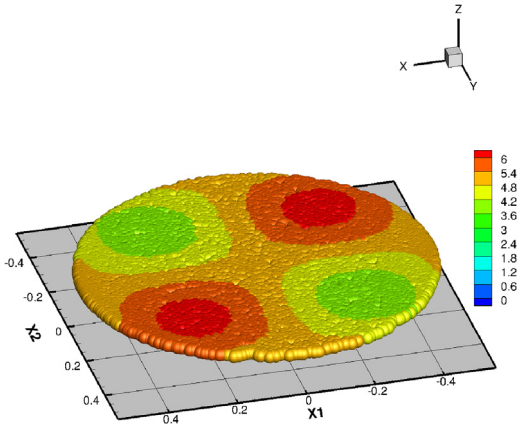

Fig. 7. For comparative purposes, the resulting point-cloud digital elevation model for a surface of $A = 0.0$. The colors indicate the *computed* refractive index (no error). (For interpretation of the references to color in this figure legend, the reader is referred to the web version of this article.)

and speed at which one needs results, this type of system is extremely difficult to simulate using continuum-based methods, such as the Finite Difference Time Domain Method or the Finite Element Method. This paper developed a fast computational method based on decomposition of the pulse into a group of rays, which are then tracked. This allows one to rapidly identify the regions where the signal will be erroneous and serves as a guide for practitioners to ascertain where problems may occur a priori to experiments. In those cases, the stereographic image would need to be reconstructed by other means, and potentially scanned from another angle and combined with other scan data.

The presented approach allows one to parametrically study the changes in scattering behavior as a function of changes in surface geometry. The simplified model captures the primary effects, reflection and absorption of optical energy, via: (1) a discretization of a concentrated optical beam into rays, (2) a discrete ray-tracking algorithm is developed to track the propagation of rays, (3) a point-cloud reproduction of the surface using time-of-flight analyses and (4) a method for material identification via inversion of the relationship between the refractive index and the measured reflectance. *The simulations take on the order of one minute on a laptop.* This type of approach is quite suitable for use in conjunction with mobile 3D body scanners, whose objective is to capture the entire human body quickly. This type of technology, coupled to mobile body-scanning devices, is a subject of current research by the author with applications focussing on prosthetic designs, analysis of biomechanical movement and surface scans for tumors.

References

[1] T.B. Moeslund, E. Granum, A survey of computer vision-based human motion capture, Comput. Vis. Image Underst. 81.3 (2001) 231–268.
[2] K.K. Biswas, S.K. Basu, Gesture recognition using microsoft kinect, Autom., Robot. Appl. (ICARA) (2001) 2011 5th International Conference on. IEEE.
[3] S. Larsson, J.A.P. Kjellander, Motion control and data capturing for laser scanning with an industrial robot, Robot. Auton. Syst. 54 (6) (2006) 453–460, http://dx.doi.org/10.1016/j.robot.2006.02.002.
[4] K.H. Strobl, E. Mair, T. Bodenmüller, S. Kielhöfer, W. Sepp, M. Suppa, D. Burschka, G. Hirzinger, The Self-Referenced DLR 3D-Modeler, in: Proceedings of the IEEE/RSJ International Conference on Intelligent Robots and Systems (IROS 2009), St. Louis, MO, USA, 2009, pp. 21–28.
[5] K.H. Strobl, E. Mair, G. Hirzinger, Image-Based Pose Estimation for 3-D Modeling in Rapid, Hand-Held Motion, in: Proceedings of the IEEE International Conference on Robotics and Automation, ICRA 2011, Shanghai, China, 2011, pp. 2593–2600.
[6] Salil Goel, Bharat Lohani, A motion correction technique for laser scanning of moving objects, IEEE Geosci. Remote Sens. Lett. (2014) 225–228.
[7] J. Ring, The laser in astronomy, New Sci. (1963) 672–673.
[8] A.P. Cracknell, L. Hayes, Introduction To Remote Sensing, second ed., Taylor and Francis, London, ISBN: 0-8493-9255-1, 2007, OCLC 70765252.
[9] G.G. Goyer, R. Watson, The laser and its application to meteorology, Bull. Am. Meteorol. Soc. 44 (9) (1963) 564–575, 568.
[10] A. Medina, F. Gaya, F. Pozo, Compact laser radar and three-dimensional camera, J. Opt. Soc. Amer. A 23 (2006) 800–805.

Please cite this article as: T.I. Zohdi, Rapid simulation-based uncertainty quantification of flash-type time-of-flight and Lidar-based body-scanning processes, Computer Methods in Applied Mechanics and Engineering (2019), https://doi.org/10.1016/j.cma.2019.03.056.

[11] P. Trickey, X. Cao, Characterization of the OPAL obscurant penetrating lidar in various degraded visual environments proc. SPIE 8737, degraded visual environments: Enhanced, synthetic, and external vision solutions 2013, 2013, 87370E, http://dx.doi.org/10.1117/12.2015259.

[12] Hansard Miles, Lee Seungkyu, Choi Ouk, Horaud Radu, Time-of-flight cameras: Principles, methods and applications, in: Briefs in Computer Science, Springer, ISBN: 978-1-4471-4657-5, 2012, http://dx.doi.org/10.1007/978-1-4471-4658-2.

[13] Schuon Sebastian, Theobalt Christian, Davis James, Thrun Sebastian, High-quality scanning using time-of-flight depth superresolution, in: IEEE Computer Society Conference on Computer Vision and Pattern Recognition Workshops, 2008 Institute of Electrical and Electronics Engineers, 2008, pp. 1–7.

[14] Gokturk Salih Burak, Yalcin Hakan, Bamji Cyrus, A Time-Of-Flight Depth Sensor - System Description, Issues and Solutions. IEEE Computer Society Conference on Computer Vision and Pattern Recognition Workshops, 2004. Institute of Electrical and Electronics Engineers, 2005, pp. 35–45, http://dx.doi.org/10.1109/CVPR.2004.291.

[15] ASC's 3D Flash LiDar camera selected for OSIRIS-REx asteroid mission, NASASpaceFlight.com, 2012-05-13.

[16] Aue Jan, Langer Dirk, Muller-Bessler Bernhard, Huhnke Burkhard, Efficient segmentation of 3D lidar point clouds handling partial occlusion, Baden-Baden, Germany, IEEE, ISBN: 978-1-4577-0890-9, 2011, http://dx.doi.org/10.1109/ivs.2011.5940442.

[17] Hsu. Stephen, Acharya Sunil, Rafii Abbas, New Richard, Performance of a time-of-flight range Camera for intelligent vehicle safety applications (PDF), in: Advanced Microsystems for Automotive Applications, VDI-Buch, Springer, ISBN: 978-3-540-33410-1, 2006, pp. 205–219, http://dx.doi.org/10.1007/3-540-33410-6-16.

[18] Elkhalili Omar, Schrey Olaf M., Ulfig Wiebke, Brockherde Werner, Hosticka Bedrich J., A 64x8 pixel 3-D CMOS time-of flight image sensor for car safety applications, in: European Solid State Circuits Conference 2006, pp. 568–571, http://dx.doi.org/10.1109/ESSCIR.2006.307488, ISBN: 978-1-4244-0302-8.

[19] H. Gross, Handbook of optical systems, in: H. Gross (Ed.), Fundamental of Technical Optics, Wiley-VCH, 2005.

[20] T.I. Zohdi, Computation of the coupled thermo-optical scattering properties of random particulate systems, Comput. Methods Appl. Mech. Engrg. 195 (2006) 5813–5830.

[21] T.I. Zohdi, F.A. Kuypers, Modeling and rapid simulation of multiple red blood cell light scattering, Proc. R. Soc. Inter. 3 (11) (2006) 823–831.

[22] T.I. Zohdi, Electromagnetic properties of multiphase dielectrics, in: A Primer on Modeling, Theory and Computation, Springer-Verlag, 2012.

[23] T.I. Zohdi, A computational modeling framework for high-frequency particulate obscurant cloud performance, Int. J. Eng. Sci. 89 (2015) 75–85.

[24] T.I. Zohdi, On high-frequency radiation scattering sensitivity to surface roughness in particulate media, Comput. Part. Mech. (2016) http://dx.doi.org/10.1007/s40571-016-0118-3.

[25] T.I. Zohdi, On the optical thickness of disordered particulate media, Mech. Mater. 38 (2006) 969–981.

[26] J.D. Jackson, Classical electrodynamics, 1998.

Please cite this article as: T.I. Zohdi, Rapid simulation-based uncertainty quantification of flash-type time-of-flight and Lidar-based body-scanning processes, Computer Methods in Applied Mechanics and Engineering (2019), https://doi.org/10.1016/j.cma.2019.03.056.